Direct imaging of the spatial and energy distribution of nucleation centres in ferroelectric materials

STEPHEN JESSE[1,2], BRIAN J. RODRIGUEZ[1,2], SAMRAT CHOUDHURY[3], ARTHUR P. BADDORF[2], IONELA VREJOIU[4], DIETRICH HESSE[4], MARIN ALEXE[4], EUGENE A. ELISEEV[5], ANNA N. MOROZOVSKA[6], JINGXIAN ZHANG[3], LONG-QING CHEN[3] AND SERGEI V. KALININ[1,2]*

[1]Materials Science and Technology Division, Oak Ridge National Laboratory, Oak Ridge, Tennessee 37831, USA
[2]The Center for Nanophase Materials Sciences, Oak Ridge National Laboratory, Oak Ridge, Tennessee 37831, USA
[3]Department of Materials Science and Engineering, Pennsylvania State University, University Park, Pennsylvania 16802, USA
[4]Max Plank Institute of Microstructure Physics, 06120 Halle, Germany
[5]Institute for Problems of Materials Science, National Academy of Science of Ukraine, 3, Krjijanovskogo, 03142 Kiev, Ukraine
[6]V. Lashkaryov Institute of Semiconductor Physics, National Academy of Science of Ukraine, 41, pr. Nauki, 03028 Kiev, Ukraine
*e-mail: sergei2@ornl.gov

Macroscopic ferroelectric polarization switching, similar to other first-order phase transitions, is controlled by nucleation centres. Despite 50 years of extensive theoretical and experimental effort, the microstructural origins of the Landauer paradox, that is, the experimentally observed low values of coercive fields in ferroelectrics corresponding to implausibly large nucleation activation energies, are still a mystery. Here, we develop an approach to visualize the nucleation centres controlling polarization switching processes with nanometre resolution, determine their spatial and energy distribution and correlate them to local microstructure. The random-bond and random-field components of the disorder potential are extracted from positive and negative nucleation biases. Observation of enhanced nucleation activity at the 90° domain wall boundaries and intersections combined with phase-field modelling identifies them as a class of nucleation centres that control switching in structural-defect-free materials.

The kinetics and thermodynamics of first-order phase transitions and the microstructure and properties of materials are universally controlled by defects[1,2]. Examples are as diversified as dislocation nucleation, motion and pinning that control mechanical properties, heterogeneous nucleation processes involved in the crystallization of metals, oxides and polymers, rain and snow formation, and nucleation centres in solid-state and electrochemical reactions. The majority of these processes involve a complex interplay between structural changes, order parameter dynamics and heat and mass exchange, thus obviating the development of a universal theoretical framework for understanding these phenomena. Ferroelectric materials provide a convenient model system for investigating the role of defects in phase transitions: a system in which bias-induced phase transition between two equivalent polarization states is reversible and is not associated with diffusion, mass or significant heat exchange and strain effects.

Defects affect the thermodynamic stability of a ferroelectric phase, and act as nucleation centres for phase transition and pinning sites for moving transformation fronts. The polarity and charge of a defect directly favours one polarization orientation (random field), whereas strain fields can destabilize the ferroelectric phase and induce transition to the non-ferroelectric state (random bond), mapping the realistic defect structure onto statistical physics models[3]. A variety of microscopy techniques have been used to observe phase stability in the vicinity of defects and to study their influence on domain wall dynamics. Dislocations shift the ferroelectric–paraelectric transition temperature and can thus account for non-switchable layers[4,5] and reduced dielectric properties[6], as confirmed by variable-temperature electron microscopy[7]. Observations of moving domain wall geometry by optical, near-field or electron microscopy provide direct information on the localization and strength of the pinning centres[8]. High-resolution electron microscopy studies enable the location of structural defects and domain walls to be established and provide insight into atomistic pinning mechanisms[9,10]. The wall roughness[11] and field dependence of the wall velocity[12] provide information on the dominant atomic-scale disorder types in the system.

Compared with wall pinning and defect-mediated phase stability, very little is known about defect-controlled nucleation mechanisms. The governing role of defects on ferroelectric domain nucleation has been recognized since the seminal work by Landauer[13]. Correspondingly, the spatial and energy distribution of nucleation centres have become a central component of statistical theories for polarization switching in macroscopic ferroelectrics[14,15]. Significant theoretical effort has been focused on the effects of surfaces[16] and passive layers[17], tunnelling-assisted
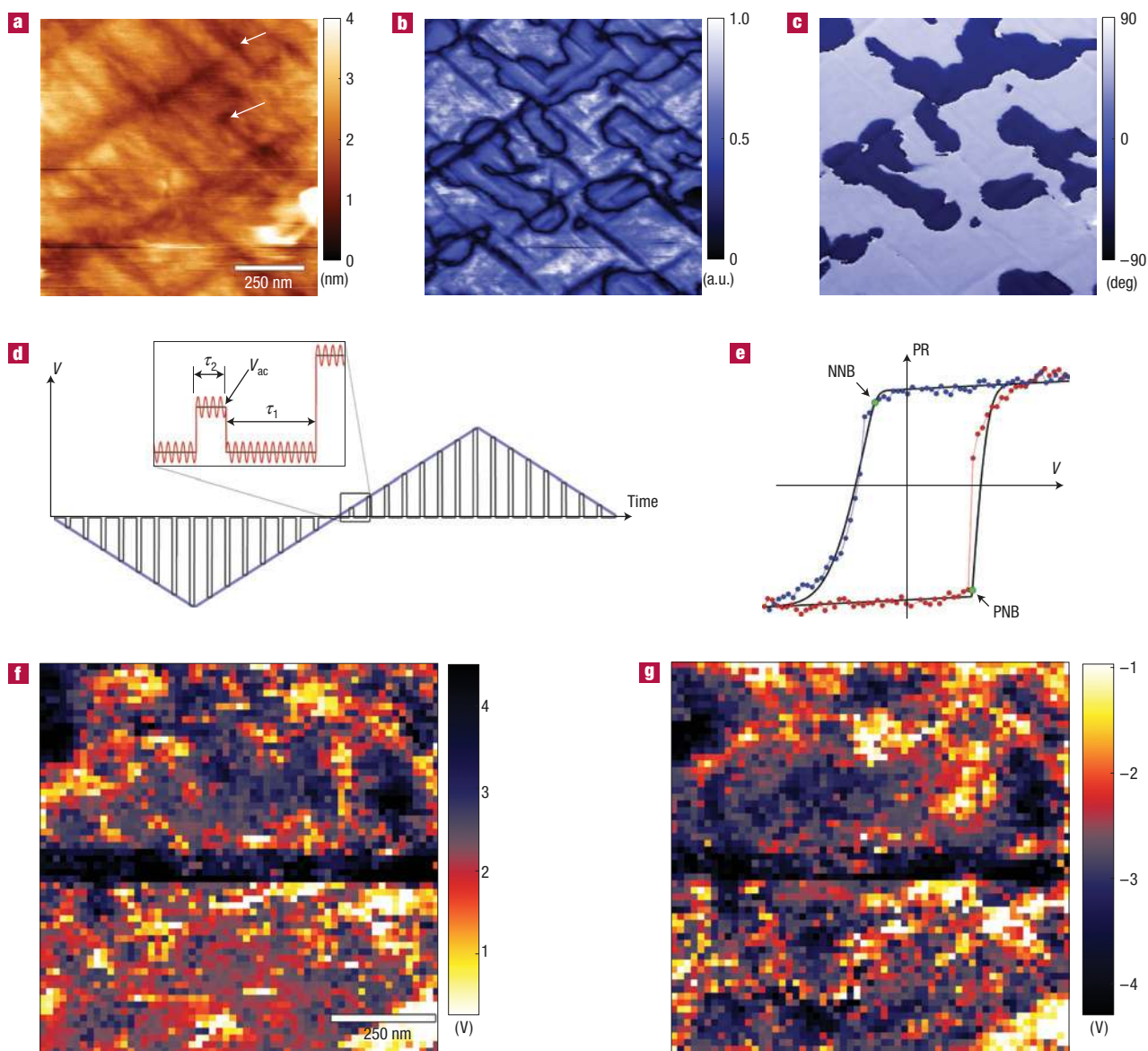
Figure 1 Imaging local nucleation biases in ferroelectric thin films. a–c, Surface topography (**a**), PFM amplitude (**b**) and PFM phase (**c**) of an epitaxial PZT film illustrating the cross-hatched pattern of in-plane a domains in a predominantly out-of-plane c-domain matrix. The regions with $-90°$ and $90°$ phase correspond to c^+ and c^- domains, respectively. Arrows indicate junctions between a_1 and a_2 domains. **d,** The voltage waveform used for local hysteresis measurements. The application of a bias results in domain nucleation below the tip, while the electromechanical response is measured using V_{ac} in the off state to minimize electrostatic contributions to the measured signal. **e,** Experimental hysteresis loop and corresponding fit illustrating positive and negative nucleation biases. **f,g,** Positive (**f**) and negative (**g**) nucleation bias maps of epitaxial PZT films. All SS-PFM maps are 960×960 nm, corresponding to 60×60 pixels at 16 nm pitch. Each pixel represents an average of three hysteresis loops. PR denotes the measured piezoresponse signal.

nucleation[18], ferroelectric–electrode coupling[19] and polar defects[20] on nucleation. However, experimental studies of specific nucleation centres remained a challenge. The characteristic size of a nucleation centre, as estimated from activation energy (typically 0.1–2 eV) is well below 10 nm. This combined with low area densities, and the fact that their effects are manifested only during a transition makes experimental observations challenging. Furthermore, nucleation is typically followed by the fast propagation of the domain wall, precluding unambiguous localization of the nucleation centre. Recent experimental studies using ultrafast focused X-ray imaging[21] and piezoresponse force microscopy[22,23] (PFM) have demonstrated

that, in a uniform field created in $\sim 100\,\mu m$ capacitor structures, the switching is initiated in a small (~ 1–10) number of locations and then propagates through the remaining (approximately tens of micrometres) region of the film. Although this process is reproducible and the defect locations can be determined repeatedly, their identity and the energetic parameters of nucleation at the defect sites and in all locations across the film are unknown.

Here, we demonstrate the real-space imaging of the energy distribution of nucleation centres in ferroelectrics, resolving the structural origins of the Landauer paradox. This approach is extended to separate the random-bond and random-field

components of the disorder potential and allows correlation to the local microstructure.

MAPPING LOCAL NUCLEATION BIASES

As a model system, we use epitaxial lead zirconate titanate film $(PbZr_{0.2}Ti_{0.8}O_3)$. Epitaxial films offer the advantage of a well-understood defect structure, which includes misfit and threading dislocations and 90° ferroelastic domain walls[24]. The latter are visible in topographic (cross-hatched patterns) and PFM images, Fig. 1a–c. The surface is relatively flat with the majority of the polarization out-of-plane (c domain) and clearly visible in-plane a domains. To map local polarization dynamics on the $\sim$10–30 nm scale, we have developed an approach based on the acquisition of multiple electromechanical hysteresis loops over an array of points on the surface[25]. Numerical analysis of the hysteresis loops extracts the positive and negative nucleation bias (PNB and NNB), as shown in Fig. 1d,e. The PNB and NNB maps in Fig. 1f,g provide a direct look into the spatial variation of switching properties across the surface. The bright regions in the nucleation images indicate where lower (absolute value) potentials are required to induce nucleation, and hence the presence of local switching centres. Conversely, dark regions correspond to regions with inhibited switching. The films are characterized by the presence of a broad spectrum of defects of various strengths and sizes. A number of $\sim$100–200 nm dark spots in Fig. 1f,g correspond to regions with inhibited switching in both directions that are probably associated with surface contaminants. A number of mesoscopic regions (3–5 pixels wide, corresponding to 50–80 nm) oriented along the [10] and [01] directions are visible, suggesting that 90° walls strongly affect domain nucleation, in agreement with earlier studies[26]. Finally, a number of 'point-like' defects are associated with a single pixel. The hysteresis loops extracted from the 'defect' points often illustrate a strong reproducible ($\sim$700 cycles for some materials) variation in the shape (fine structure) from the ideal surface. These spots are probably associated with single dislocation dipoles or other one-dimensional (1D) defects that are present in sufficient concentrations ($\sim$10^{14} m^{-2}) and can affect the activation energy for nucleation significantly.

The PNB and NNB maps are directly linked to the random-bond and random-field components of the defect-induced disorder potential, providing an approach to separate the two. The random-bond defects do not break the symmetry between equivalent polarization states, but instead increase or decrease the height of the potential barrier between the two. In the limit of a zero potential barrier, they correspond to a transition from a ferroelectric phase to a cubic, nonpolar phase. A signature of the random-bond defects on the PNB/NNB maps is that they facilitate or impede nucleation equally for both positive and negative polarities (Fig. 2a). The random-field defects break the symmetry between equivalent polarization states, leading to polarization imprint and, in extreme cases, to a polar non-ferroelectric phase (for example, regions with frozen polarization). On the PNB/NNB images, the random-field defects will facilitate nucleation in one direction while inhibiting nucleation in the reverse direction, Fig. 2b. The spatial distribution of the random-bond and random-field disorder components is illustrated in Fig. 3a. A purely symmetric distortion of a local hysteresis loop relative to the average (random bond) is mapped to a grey scale where white and black is a decrease and increase in the absolute value of nucleation bias, respectively. A purely antisymmetric distortion, or lateral shift, of a hysteresis loop (random field) is represented as a red–blue gradient, where red represents positive lateral shift of a hysteresis loop $(-3.5 < \Delta PNB < 2.8, -5 < \Delta NNB < 3.1$ (V)). Hysteresis loops corresponding to selected locations with either
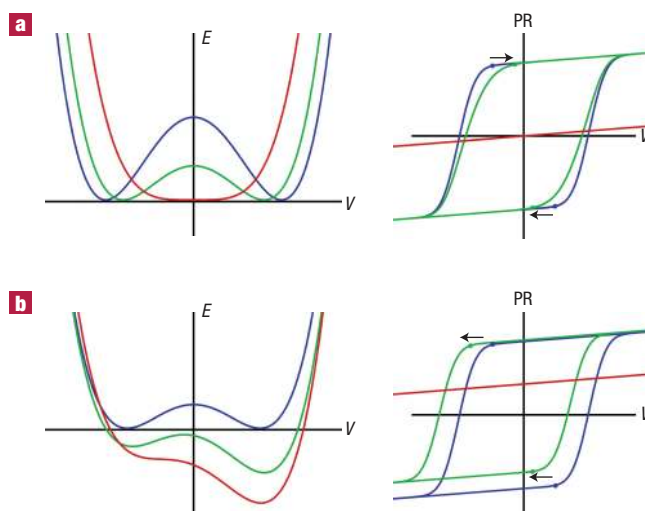

Figure 2 The role of defects on the energetics of polarization switching.
a,b, Random-bond (symmetric) (**a**) and random-field (asymmetric) (**b**) disorder in a ferroelectric material and their effects on local hysteresis loop shape. The blue curves correspond to a defect-free material, green curves to the presence of a weak random-bond (**a**) and random-field (**b**) defect, and red curves to the limiting cases of a nonpolar phase and polar non-ferroelectric phases, respectively.

predominantly random-bond or random-field disorder are shown in Fig. 3b,c.

ROLE OF DISORDER ON TIP-INDUCED SWITCHING

The PNB and NNB maps are directly related to the surface and bulk microstructures of materials, necessitating the interpretation of the switching data in terms of local properties. For the case when effective material properties, such as spontaneous polarization and built-in electric field, vary slowly over the length scale of the nucleating domain ($\sim$0.4–2 nm, as estimated from the activation energy), the relationship between switching behaviour and local material properties can be established using a modified Landauer–Molotskii thermodynamic model[27]. The free energy of a nucleating semi-ellipsoidal domain of radius, r, and length, l, is

$$\Phi(r, l, U) = U\Phi_U(r, l) + \Phi_S(r, l) + \Phi_D(r, l),$$

where $U\Phi_U(r, l)$ is the interaction energy between the tip under applied bias, U, and the sample polarization, $\Phi_S(r, l)$ is the domain wall energy and $\Phi_D(r, l)$ is the depolarization field energy. The critical bias for nucleation is derived as[28] (see the Supplementary Information):

$$U_{cr} \approx 4\sqrt{\frac{d\psi_S\gamma}{3\varepsilon_0(\kappa + \varepsilon_e)}},$$

where the domain wall energy is ψ_S, the effective dielectric constant is $\kappa = \sqrt{\varepsilon_{11}\varepsilon_{33}}$ and the dielectric anisotropy is $\gamma = \sqrt{\varepsilon_{11}/\varepsilon_{33}}$; ε_e is the dielectric constant of the ambient environment. The tip geometry is described by a characteristic tip size, d, that can be determined self-consistently from domain wall width[29]. Corresponding domain parameters are $l(U_{cr}) = 2\gamma d$ and $r(U_{cr}) \approx \pi\sqrt{3\varepsilon_0\gamma(\kappa + \varepsilon_e)\psi_S d}/4P_S$, where P_S is the spontaneous polarization.

The kinetics of the switching process can be deduced from the structure of the free-energy surface within the framework of
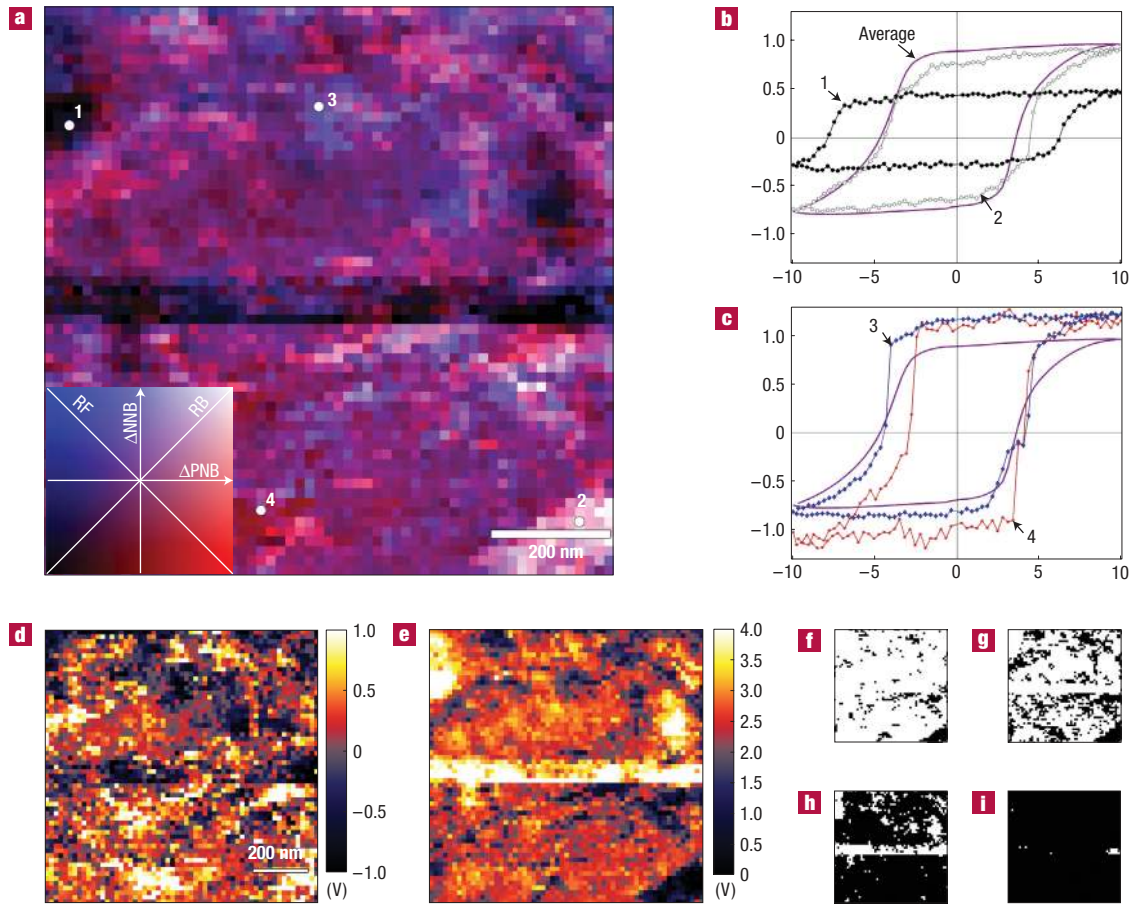
Figure 3 Reconstruction of random-field and random-bond disorder components. a, Random-field (RF) and random-bond (RB) disorder map. The axes on the colour map are defined as $\triangle PNB = -PNB + \langle PNB \rangle$ and $\triangle NNB = NNB - \langle NNB \rangle$, which are the local deviations of the positive and negative nucleation biases from their global averages. The diagonals of the colour map indicate correlations between $\triangle PNB$ and $\triangle NNB$, that is, the relative degrees of random field and random bond. **b,c**, Example loops of random-bond (**b**) and random-field (**c**) disorder from locations indicated in **a**. The violet solid line corresponds to the average hysteresis loop across the film. **d,e**, The domain-wall (**d**) and built-in field (**e**) parts of the disorder potential obtained from the data in Fig. 1f,g. Note that the change in the tip state (presumably due to a particle pick-up) strongly affects the symmetric (wall width/polarization magnitude) part, but affects the antisymmetric (built-in potential) component only weakly. **f–i**, The spatial distribution of switching sites active for a tip bias of 1 V (**f**), 3 V (**g**), 5 V (**h**) and 7 V (**i**). Black indicates locations where the local activation energy for nucleation at a given voltage is below $20 K_b T$, corresponding to the onset of thermal nucleation.

activation rate theory. The nucleation time is related to activation energy as $\tau(U) \sim \tau_0 \exp(E_a/kT)$, where the attempt time is $\tau_0 \approx 10^{-13}$ s, k is the Boltzmann constant and T is absolute temperature. The activation energy for domain formation, $E_a(U)$, corresponding to the saddle point on the $\Phi(r, l)$ surface for a given tip bias U, is

$$E_a(U) = \frac{2}{3\varepsilon_0(\kappa + \varepsilon_e)P_S}\left(\frac{\pi\psi_S d\gamma}{U + 2d\gamma E_S}\right)^3 = \frac{E^*}{(U + 2d\gamma E_S)^3}.$$

Here E_S is the built-in electric field in the surface layer. For typical experimental conditions, the onset of nucleation occurs when $\tau(U) \leq 10^{-3}$ s, corresponding to $U > \sqrt[3]{E^*/20kT} - 2d\gamma E_S$.

RECONSTRUCTION OF THE DISORDER POTENTIAL COMPONENTS

The random-field and random-bond disorder in a material can be related to the presence of a surface built-in field, E_S (random field), variation in wall energy, $\psi_S(x,y) = \psi_S^0 \alpha(x,y)$ (random

bond), or built-in frozen polarization, $P_S(x,y) = P_S^0(1 + \beta(x,y))$ (random field). Here, ψ_S^0 and P_S^0 correspond to the parameters of an ideal material, and $\alpha(x,y)$ and $\beta(x,y)$ describe the deviation from an ideal material. Assuming that the tip properties, A, are position independent, the positive and negative nucleation biases are derived as

$$PNB = U_+ = -2d\gamma E_S + \frac{A\psi_S^0 \alpha(x,y)}{\sqrt[3]{P_S^0(1 + \beta(x,y))}} \qquad (1a)$$

$$NNB = U_- = -2d\gamma E_S - \frac{A\psi_S^0 \alpha(x,y)}{\sqrt[3]{P_S^0(1 - \beta(x,y))}}. \qquad (1b)$$

The nucleation bias data in Fig. 1f,g are analysed using equations (1a) and (1b) for the cases of $\beta(x,y) = 0$ and $E_S = 0$. In the first case, the built-in surface potential $2d\gamma E_S(x,y)$ and random-bond polarization disorder, $A\psi_S^0 \alpha(x,y)/\sqrt[3]{P_S^0}$, are reconstructed as shown in Fig. 3d,e. Note that the change in the tip state (band in the centre of the
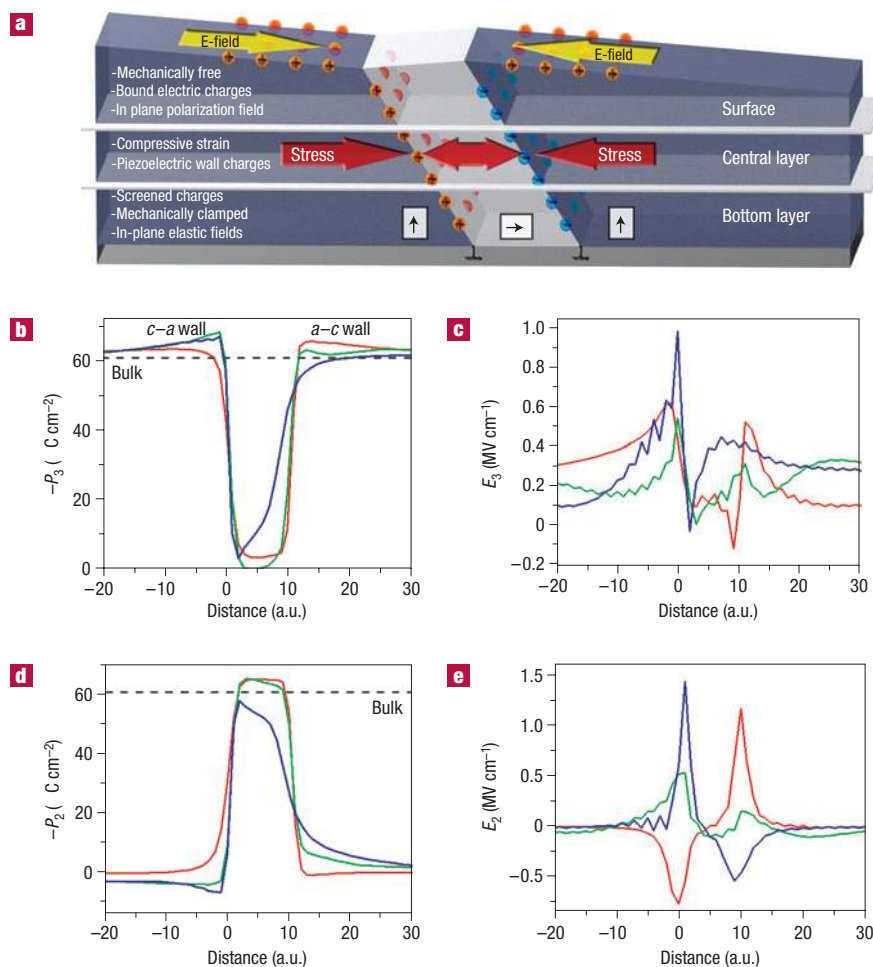
Figure 4 Phase-field modelling of the domain structure and polarization and field distributions in the vicinity of the ferroelastic domain. a, Schematic diagram of a single *a* domain in a *c* matrix and spatial distributions of electric charges at the top, middle and bottom of the film. **b–e**, Corresponding polarization profiles (**b,d**) and built-in electric fields (**c,e**) for the surface (red), centre (green) and bottom (blue) layers.

image) affects random-bond (dielectric gap), but not random-field properties. From comparison of the scales in Fig. 3d,e, the random-field disorder is significantly smaller than random-bond disorder. In the second case, reconstruction gives an extremely broad distribution for the frozen polarization component, $\beta(x, y) = 0.2 \pm 0.8$, which may be consistent with a surface dead layer. Remarkably, the random-bond disorder components in both cases are virtually identical, suggesting that the deconvolution procedure is reliable. From thus determined materials parameters, the localization of the nucleation sites active for each voltage can be visualized as shown in Fig. 3f–i. Here, black regions illustrate locations at which switching will be initiated for a given potential. In comparison, in a plane-capacitor experiment, domain growth initiated at low-coercivity sites will overrun and mask switching conditions at high-coercivity sites, thus preventing any observation of the local switching parameters[21].

ROLE OF LOCALIZED DEFECTS ON NUCLEATION: FERROELASTIC WALLS

In addition to long-range variations in effective properties, the films are characterized by the presence of localized defects such as ferroelastic domain walls and dislocations. As observed experimentally, the ferroelastic in-plane *a* domains formed by 90°

wall pairs and especially a_1–a_2 junctions act as efficient nucleation centres for 180° domain switching. To analyse the role of these defects in polarization switching, we use phase-field modelling to study the multiple, interacting mechanisms operating during ferroelastic wall-mediated nucleation. The evolution of the 3D polarization field (P_1, P_2, P_3) is described by time-dependent Ginzburg–Landau equations

$$\frac{\partial P_i(\mathbf{x}, t)}{\partial t} = -L \frac{\delta F}{\delta P_i(\mathbf{x}, t)}, \quad i = 1, 2, 3,$$

where L is a kinetic coefficient related to the domain wall mobility and F is the total free energy of the system including bulk, domain wall, elastic energy and electrostatic contributions (see the Supplementary Information).

Relaxation of the random polarization distribution for a defined lattice mismatch and grounded bottom electrode and free top surface yields an *a–c* domain structure closely resembling that observed experimentally. Beyond domain morphology, the phase-field data provide direct insight into the electric and elastic fields and polarization distributions, as shown in Fig. 4. Note that the *a*-domain width is determined by the free-energy minimum and thicker *a* domains (for which two walls will be far apart) are not stable. The built-in electric field in the centre of the
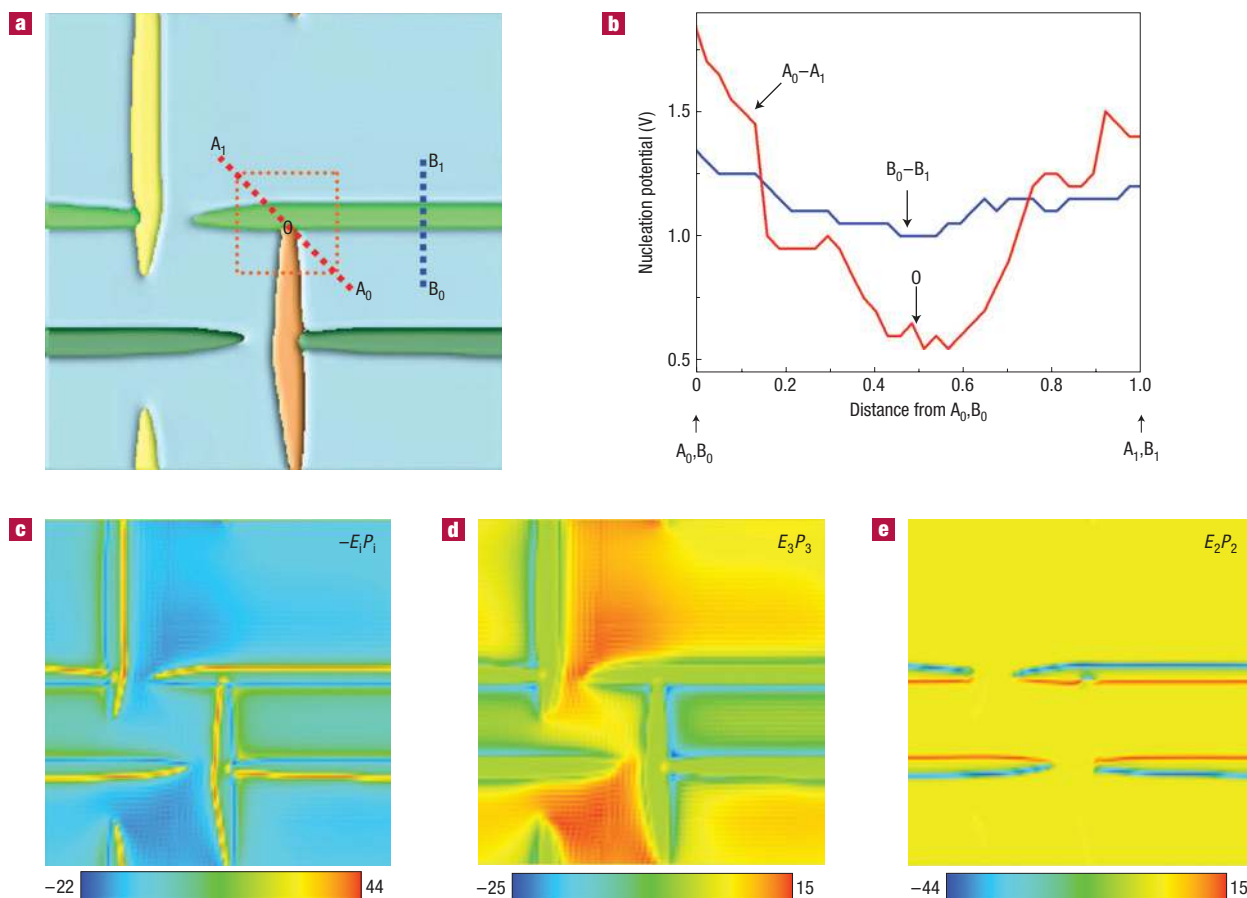
Figure 5 Phase-field modelling of the effect of domain boundaries on nucleation bias. **a,b**, Domain structure of PZT film (**a**) and distribution of nucleation potential (**b**) along the profiles ($A_0–A_1$ and $B_0–B_1$). **c–e**, Maps of the free-energy components corresponding to full electrostatic energy (**c**) and E_3P_3 (**d**) and E_2P_2 (**e**) components. Units are $J\,cm^{-3}$.

film is almost antisymmetric, as can be anticipated from the charge distribution induced by compressive strain across the a domain due to the direct piezoelectric effect. On the surface, the polarization charge variation between a ($\sigma = 0$) and c ($\sigma = P$) domains results in a large in-plane electric field, accommodated by ferroelectric nonlinearity (depolarization effect), resulting in asymmetric electric field distributions and wall broadening[30]. Finally, the 90° wall–interface junctions form strain dipoles due to substrate clamping, with associated elastic and electrostatic fields. These mechanisms are acting simultaneously, and thus can be captured only by a full 3D model.

The built-in electric fields and stress fields at the domain wall directly control the switching mechanism. The application of a uniform electric field across the film in the phase-field model indicates that switching is always initiated at the $a–c$ wall–interface junction, which thus serves as the dominant switching centre. An increase of the electric field results in rapid growth of the domain, which eventually spans the film. This rapid growth is a dominant aspect in experimental studies of switching in capacitor structures, in which a single defect dominates the dynamics of the whole structure. Hence, modelling (or experiment) in a uniform field maps only the preferred nucleation centre, but not the variations in nucleation energies.

In contrast, in a PFM experiment (without top electrodes), the electric field is applied locally, allowing the nucleation process to

be probed within a selected volume. To model this process, the tip-induced potential distribution is approximated by the Lorentz function, $\phi_1(x, y) = \phi_0 c^2/(r^2 + c^2)$, where r is the distance from the tip–surface junction and c is the characteristic extent of the electric field of the tip. From the observed 180° domain wall width, c is estimated as 10–30 nm, corresponding to a nucleation bias of the order of ~2–3 V for an ideal surface. An assessment of experimentally measured and modelled nucleation biases indicates that, in regions away from domain walls, the large non-uniform electric field of the PFM tip is sufficient to induce intrinsic polarization switching.

To establish the role of ferroelastic walls and $a_1–a_2$ domain junctions on switching in a PFM experiment, the variations of nucleation potential along the selected microstructural elements are plotted in Fig. 5a,b. The nucleation potential is lower near a domain wall or an intersection of domain walls, and is reduced to ~0.5 V at the domain junction as compared with ~2 V for the free film. These results compare favourably to experimental measurements, which yield ~3 V potential for nucleation on the defect-free regions and 0.2–0.5 V for nucleation bias at the defects. This agreement proves that wall junctions act as strong nucleation centres, and in the absence of other defects will determine polarization dynamics in thin films. The threshold lowering mechanism can be understood from phase-field modelling by calculating the maps of free energies corresponding

to strain, in-plane and out-of-plane field components as shown in Fig. 5c–e (ref. 31). The nucleation potential is lowered by the built-in vertical electric field at the domain wall (compare Fig. 4) and the strain fields that lower the domain wall energy as demonstrated by wall broadening. The extra contribution to nucleation behaviour originates from the coupling of the in-plane polarization component, P_2, to the in-plane component of the electric field E_2, produced by the tip, which facilitates switching at the a–c walls and impedes switching at the c–a walls. However, the general mechanisms for nucleation potential lowering in the uniform and local field case are similar.

SUMMARY

Understanding the switching behaviour in ferroelectrics on the nanometre scale is directly relevant to the development and optimization of applications such as non-volatile random-access memories[32,33], ferroelectric tunnel junctions[34] and high-density data storage[35,36]. The combined switching spectroscopy PFM (SS-PFM)—phase-field modelling approach can be extended to defects of other types, including misfit and threading dislocations with defined Burgers vectors, antiphase boundaries or grain boundaries. The use of systems with engineered defect structures such as bicrystal grain boundaries or periodic dislocation arrays, or combined electron microscopy/PFM studies will extend these measurements to well-defined structural defects.

Beyond polarization switching in ferroelectrics, this approach can be extended to studies of the role of defects on the thermodynamics and kinetics of other local reversible voltage-induced transitions, including phase-change materials and electrochemical reactions. This will provide a universal framework for studying the role of defects in nucleation and growth of new phases and in electrochemical reaction kinetics one defect at a time, opening a pathway to understand the structure–property relationships of defect sites, and hence the optimization and control of these processes.

METHODS

MATERIALS

Epitaxial lead zirconate titanate films ($PbZr_{0.2}Ti_{0.8}O_3$) are grown by pulsed laser deposition to a 200 nm thickness on a (001) $SrRuO_3$ electrode. The detailed preparation conditions are described in Supplementary Information.

EXPERIMENTAL SET-UP

SS-PFM is implemented on a commercial scanning probe microscope system (Veeco MultiMode with Nanoscope-IIIA controller) equipped with external data-acquisition electronics based on an NI-6115 fast data-acquisition card to generate the probing signal and store local hysteresis loops and correlate them with surface topography.

NUCLEATION BIAS MAPPING

In SS-PFM, the probe concentrates an electric field to a nanoscale volume of material ($\sim$10–50 nm) and induces local domain nucleation and growth. Simultaneously, the d.c.-field-induced changes in the local polarization orientation are determined via detection of the electromechanical response of the material to a small a.c. bias (1–2 V_{pp}, 1–2 MHz). When the d.c. bias reaches the local nucleation bias, a domain forms and this onset of nucleation corresponds to the point in the hysteresis loop where the signal deviates from a constant value by a set-point value of 3%. The hysteresis loop acquisition is carried out on a square grid to yield a 3D data array.

PHASE-FIELD MODELLING

Time-dependent Ginzburg–Landau equations are solved using the semi-implicit Fourier spectral method on $128\Delta x \times 128\Delta x \times 36\Delta x$ mesh with periodic boundary conditions along the x_1 and x_2 axes. Film thickness is $h_f = 20\Delta x$. The bulk free-energy and electrostrictive coefficients used are

listed in Supplementary Information. The elastic constants are used for cubic anisotropy for PbTiO$_3$: $c_{11} = 1.75 \times 10^{11}$ N m^{-2}, $c_{12} = 7.94 \times 10^{11}$ N m^{-2} and $c_{44} = 1.11 \times 10^{11}$ N m^{-2}. The substrate strain is $\varepsilon^0_{11} = \varepsilon^0_{22} = -0.003$, and the gradient energy coefficients $G_{11}/G_{110} = 0.6$ for the simulation. To find the critical nucleation potential, the potential ϕ_0 is increased gradually with a 0.05 V step until the formation of a new domain is detected.

References

1. Binder, K. Theory of 1st-order phase-transitions. *Rep. Prog. Phys.* **50**, 783–859 (1987).
2. Chaikin, P. M. & Lubensky, T. C. *Principles of Condensed Matter Physics* (Cambridge Univ. Press, Cambridge, 1995).
3. Nattermann, T., Shapir, Y. & Vilfan, I. Interface pinning and dynamics in random-systems. *Phys. Rev. B* **42**, 8577–8586 (1990).
4. Nagarajan, V. *et al.* Misfit dislocations in nanoscale ferroelectric heterostructures. *Appl. Phys. Lett.* **86**, 192910 (2005).
5. Balzar, D., Ramakrishnan, P. A. & Hermann, A. M. Defect-related lattice strain and the transition temperature in ferroelectric thin films. *Phys. Rev. B* **70**, 092103 (2004).
6. Canedy, C. L. *et al.* Dielectric properties in heteroepitaxial Ba$_{0.6}$Sr$_{0.4}$TiO$_3$ thin films: Effect of internal stresses and dislocation-type defects. *Appl. Phys. Lett.* **77**, 1695–1697 (2000).
7. Wang, R. H., Zhu, Y. M. & Shapiro, S. M. Structural defects and the origin of the second length scale in SrTiO$_3$. *Phys. Rev. Lett.* **80**, 2370–2373 (1998).
8. Yang, T. J., Gopalan, V., Swart, P. J. & Mohideen, U. Direct observation of pinning and bowing of a single ferroelectric domain wall. *Phys. Rev. Lett.* **82**, 4106–4109 (1999).
9. Emelyanov, A. Y. & Pertsev, N. A. Abrupt changes and hysteretic behavior of 90 degrees domains in epitaxial ferroelectric thin films with misfit dislocations. *Phys. Rev. B* **68**, 214103 (2003).
10. Chu, M. W., Szafraniak, I., Hesse, D., Alexe, M. & Gosele, U. Elastic coupling between 90 degrees twin walls and interfacial dislocations in epitaxial ferroelectric perovskites: A quantitative high-resolution transmission electron microscopy study. *Phys. Rev. B* **72**, 174112 (2005).
11. Paruch, P., Giamarchi, T. & Triscone, J. M. Domain wall roughness in epitaxial ferroelectric PbZr$_{0.2}$Ti$_{0.8}$O$_3$ thin films. *Phys. Rev. Lett.* **94**, 197601 (2005).
12. Tybell, T., Paruch, P., Giamarchi, T. & Triscone, J. M. Domain wall creep in epitaxial ferroelectric Pb(Zr$_{0.2}$Ti$_{0.8}$)O$_3$ thin films. *Phys. Rev. Lett.* **89**, 097601 (2002).
13. Landauer, R. Electrostatic considerations in BaTiO$_3$ domain formation during polarization reversal. *J. Appl. Phys.* **28**, 227–234 (1957).
14. Ishibash, Y. & Takagi, Y. Ferroelectric domain switching. *J. Phys. Soc. Japan* **31**, 506–510 (1971).
15. Scott, J. F. *et al.* Switching kinetics of lead zirconate titanate sub-micron thin-film memories. *J. Appl. Phys.* **64**, 787–792 (1988).
16. Ahluwalia, R. & Cao, W. W. Influence of dipolar defects on switching behavior in ferroelectrics. *Phys. Rev. B* **63**, 012103 (2001).
17. Bratkovsky, A. M. & Levanyuk, A. P. Easy collective polarization switching in ferroelectrics. *Phys. Rev. Lett.* **85**, 4614–4617 (2000).
18. Molotskii, M., Kris, R. & Rosenman, G. Fluctuon effects in ferroelectric polarization switching. *J. Appl. Phys.* **88**, 5318–5327 (2000).
19. Gerra, G., Tagantsev, A. K. & Setter, N. Surface-stimulated nucleation of reverse domains in ferroelectrics. *Phys. Rev. Lett.* **94**, 107602 (2005).
20. Ahluwalia, R. & Cao, W. W. Effect of surface induced nucleation of ferroelastic domains on polarization switching in constrained ferroelectrics. *J. Appl. Phys.* **93**, 537–544 (2003).
21. Grigoriev, A. *et al.* Nanosecond domain wall dynamics in ferroelectric Pb(Zr, Ti)O$_3$ thin films. *Phys. Rev. Lett.* **96**, 187601 (2006).
22. Gruverman, A. *et al.* Direct studies of domain switching dynamics in thin film ferroelectric capacitors. *Appl. Phys. Lett.* **87**, 054107 (2005).
23. Kim, D. J. *et al.* Observation of inhomogeneous domain nucleation in epitaxial Pb(Zr, Ti)O$_3$ capacitors. *Appl. Phys. Lett.* **91**, 132903 (2007).
24. Vrejoiu, I. *et al.* Threading dislocations in epitaxial ferroelectric PbZr$_{0.2}$Ti$_{0.8}$O$_3$ films and their effect on polarization backswitching. *Phil. Mag.* **86**, 4477–4486 (2006).
25. Jesse, S., Lee, H. N. & Kalinin, S. V. Quantitative mapping of switching behavior in piezoresponse force microscopy. *Rev. Sci. Instrum.* **77**, 073702 (2006).
26. Ganpule, C. S. *et al.* Imaging three-dimensional polarization in epitaxial polydomain ferroelectric thin films. *J. Appl. Phys.* **91**, 1477–1481 (2002).
27. Molotskii, M. *et al.* Ferroelectric domain breakdown. *Phys. Rev. Lett.* **90**, 187601 (2003).
28. Morozovska, A. N. *et al.* Piezoresponse force spectroscopy of ferroelectric-semiconductor materials. *J. Appl. Phys.* **102**, 114108 (2007).
29. Kalinin, S. V. *et al.* Quantitative determination of tip parameters in piezoresponse force microscopy. *Appl. Phys. Lett.* **90**, 212905 (2007).
30. Ponomareva, I., Naumov, II & Bellaiche, L. Low-dimensional ferroelectrics under different electrical and mechanical boundary conditions: Atomistic simulations. *Phys. Rev. B* **72**, 214118 (2005).
31. Choudhury, S., Li, Y. L., Krill, C. & Chen, L. Q. Effect of grain orientation and grain size on ferroelectric domain switching and evolution: Phase field simulations. *Acta Mater.* **55**, 1415–1426 (2007).
32. Scott, J. F. *Ferroelectric Memories* (Springer, Berlin, 2000).
33. Waser, R. *Nanoelectronics and Information Technology* (Wiley-VCH, Weinheim, 2003).
34. Tsymbal, E. Y. & Kohlstedt, H. Applied physics—Tunneling across a ferroelectric. *Science* **313**, 181–183 (2006).
35. Tybell, T., Ahn, C. H. & Triscone, J. M. Control and imaging of ferroelectric domains over large areas with nanometer resolution in atomically smooth epitaxial Pb(Zr$_{0.2}$Ti$_{0.8}$)O$_{-3}$ thin films. *Appl. Phys. Lett.* **72**, 1454–1456 (1998).
36. Cho, Y., Hashimoto, S., Odagawa, N., Tanaka, K. & Hiranaga, Y. Nanodomain manipulation for ultrahigh density ferroelectric data storage. *Nanotechnology* **17**, S137—S141 (2006).